

Banner appropriate to article type will appear here in typeset article

Structures of elastoinertial turbulence in pipe flow

Manish Kumar¹† and Michael D. Graham¹

¹Department of Chemical and Biological Engineering, University of Wisconsin-Madison, 1415 Engineering Dr, Madison, WI 53706, USA

Elastoinertial turbulence (EIT) is a self-sustaining chaotic state resulting from the interplay between inertia and elasticity in the flow of dilute polymeric solutions, and its emergence is believed to limit the achievable drag reduction in turbulence flow using polymer additives. In the present study, we introduce a viscoelastic variant of spectral proper orthogonal decomposition (VESPOD) that decomposes velocity and polymeric stress fields of EIT together into well-defined orthogonal oscillating modes such that the decomposition is optimal in the terms of the total mechanical energy of the flow. Using this technique, we investigate the dominant coherently evolving structures underlying the dynamics of EIT in axisymmetric pipe flow. By analyzing distinct peaks in the leading eigenvalue of the VESPOD eigenvalue spectrum, we find that the dynamics of EIT in pipe flow is dominated by three distinct families of traveling waves, where the higher wavenumber structures of each family are simple harmonics of their respective fundamental waves. The radial velocity fields of the traveling waves are characterized by the formation of large-scale structures spanning the pipe radial direction. However, the polymeric stress fields corresponding to them are characterized by the formation of thin inclined sheets of high stress fluctuations at the critical layers of the respective waves, i.e. the locations where the wave speed of the VESPOD mode matches the mean streamwise velocity. Additionally, these sheets exhibit nested structures, where the polymeric sheets of faster waves are confined by those of the immediately slower waves.

1. Introduction

The reduction of turbulent drag using polymer additives has been an active area of research due to its application to save energy during liquid transport (Xi 2019) ever since it was discovered that the addition of a tiny amount ($\sim O(10)$ ppm) of high molecular weight polymer suppresses inertial turbulence and dramatically reduces frictional drag (Toms 1949). Although polymer additives can significantly reduce frictional drag, the flow does not become laminar; hence, the drag is always higher than the laminar value. This phenomenon is attributed to the presence of a self-sustaining weakly fluctuating flow state known as the Maximum Drag Reduction (MDR) asymptote (Virk *et al.* 1970). At MDR, the frictional drag is nearly independent of the type and concentration of polymers; understanding MDR is an important area of research because it sets a limit for attainable amount of drag reduction. Earlier studies of MDR mainly focused on the ensemble statistics of the velocity fluctuations, however, recent advancements in the field attempt to understand the dynamic evolution of

† Email address for correspondence: manish030297@gmail.com

the MDR state (Xi 2019). The discovery of elastoinertial turbulence (EIT), a self-sustaining chaotic state resulting from the interplay between inertia and elasticity, provides some understanding of the dynamics of the MDR state (Samanta *et al.* 2013; Datta *et al.* 2022; Dubief *et al.* 2023). In this paper, we investigate the dynamics of EIT in pipe flow and discover dominant structures underlying its dynamics.

Elastoinertial turbulence can sustain in the parameter regime characterized by the Reynolds number Re (dimensionless number representing the ratio of inertial to viscous forces) and the Weissenberg number Wi (product of polymer relaxation time to characteristic strain rate), where the flow is linearly stable, suggesting a nonlinear route for transition to EIT. Viscoelastic channel flow becomes linearly unstable due to a wall mode instability at sufficiently large Re (Zhang *et al.* 2013) and a center mode instability at a large Wi (Page *et al.* 2020; Khalid *et al.* 2021), the parameter values significantly higher than the EIT parameter regime of interest here. The wall mode instability leads to the emergence of a traveling wave known as the “Tollmien–Schlichting (TS)” wave (Drazin & Reid 1981), and the center mode instability leads to the emergence of another distinct traveling wave having an “arrowhead” structure (Page *et al.* 2020). The origins of these traveling waves are highly subcritical, and they can persist subcritically to the parameter regimes relevant to EIT. Inspired by these facts, it was speculated that the non-linear excitation of either the wall mode (Shekar *et al.* 2019, 2020, 2021) or the center mode (Page *et al.* 2020; Dubief *et al.* 2022) could lead to EIT. Recent advancements indicate that in elastoinertial regime, wall-mode structures dominate the dynamics (Kumar & Graham 2024; Kumar *et al.* 2025; Beneitez *et al.* 2024a), while at vanishing Re , the dynamics tend to be organized around the center mode structures (Morozov 2022; Beneitez *et al.* 2024b; Lewy & Kerswell 2025).

Recently, using spectral proper orthogonal decomposition (SPOD) (Towne *et al.* 2018), we have revealed the dominant coherent structures underlying the dynamics of EIT in channel flow (Kumar & Graham 2024). The SPOD is a temporal variant of the proper orthogonal decomposition (POD) (Holmes *et al.* 2012) and decomposes time-dependent state variables into oscillating orthogonal basis functions such that the basis functions are coherent in both space and time. We demonstrated that the dynamics of EIT in channel flow is predominantly composed of a family of non-harmonic traveling waves, where the most dominant traveling wave of the family resembles the structure of the Tollmien–Schlichting (TS) wave (Kumar & Graham 2024). The wall-normal velocity of the most dominant traveling wave has large-scale regular structures spanning the channel height, the streamwise velocity component has regular structures in the vicinity of the channel walls, and the polymeric stress field contains thin sheets of high polymeric stress fluctuations localized at the critical layers of the traveling wave. The critical layer is the location where the wave speed of the traveling wave matches the mean streamwise velocity. The remaining traveling waves of the family exhibit similar structures, however nested in the region bounded by the polymeric sheets and hence critical layers of immediately slower traveling wave. The sheets of high polymeric stress act as barriers for flow and hence prevent velocity fluctuations from penetrating them (Kumar *et al.* 2023). Thus, the dynamics of EIT in channel flow originates from a nonlinear excitation of a wall mode and is dominated by a family of self-similar nested traveling waves where the polymeric sheets of each traveling wave confines the velocity fluctuations of their immediate faster wave. Strengthening the notion of the connection of EIT with wall mode, it has also been found that the arrowhead structure resulting from the center mode instability is disconnected from EIT, and it does not play a role in the self-sustenance of the dynamics of EIT (Beneitez *et al.* 2024a).

The investigation of the dynamics of EIT in pipe flow has received relatively little attention (Lopez *et al.* 2019; Choueiri *et al.* 2021) and is the topic of the present study. Similar to channel flow, the center mode becomes linearly unstable even in viscoelastic pipe flow

at $Re = O(100)$ and $Wi = O(10)$ (Garg *et al.* 2018; Chaudhary *et al.* 2021). Weakly nonlinear analysis around the linearly unstable center-mode demonstrates that nonlinearity stabilizes the flow at high polymer concentration while it destabilizes the flow at low polymer concentration, indicating supercritical and subcritical bifurcations at high and low polymer concentrations, respectively (Wan *et al.* 2021). In contrast, the wall mode in the pipe flow remains linearly stable at all Re . However, using resolvent analysis, it has been found that the structure of the most strongly amplified mode in viscoelastic pipe flow contains strong stress fluctuations localized at the critical layer (Zhang 2021), similar to the viscoelastic channel flow (Shekar *et al.* 2019), indicating a critical layer mechanism of the dynamics of EIT even in pipe flow. Further, there are common characteristics of the structures of EIT in both channel and pipe flows. For example, EIT in both channel and pipe flows exhibits near-wall vortical structures oriented in the direction perpendicular to the mean flow direction and near-wall elongated streaks of streamwise velocity fluctuations aligned in the flow direction with a slight slope (Samanta *et al.* 2013; Lopez *et al.* 2019; Choueiri *et al.* 2021).

The basic characteristics of EIT in channel and pipe flows are fundamentally two-dimensional (2-D) (Sid *et al.* 2018; Lopez *et al.* 2019). Therefore, in the present study, we investigate the dynamics of EIT in axisymmetric pipe flow. We perform direct numerical simulations of EIT using a spectral method. To analyze the dynamics, we introduce a viscoelastic variant of the SPOD (Towne *et al.* 2018), which we refer to as “VESPOD”, that enables us to investigate the well-defined structures underlying EIT that evolve coherently in time. As detailed below, VESPOD is based on the total mechanical energy (kinetic plus elastic) of the flow, enabling an energy-based modal decomposition that contains both velocity and polymer stress fields. The eigenvalue spectrum of VESPOD exhibits distinct peaks and by analyzing those peaks we find that the dynamics of EIT in pipe flow, in the parameter regime studied, is dominated by three distinct families of traveling waves. We also explore the effects of the domain length, Re , and Wi on the dynamics of EIT and the traveling waves underlying its dynamics and comment on the relation between EIT in pipe and channel flow. The remaining part of the paper has been organized as follow: Section 2 discusses the methodology, Section 3 focuses on results and discussion, and Section 4 concludes the finding of the study and discusses the relationship between EIT in the pipe and channel flow.

2. Formulation and governing equations

2.1. Direct numerical simulation of EIT

The flow is governed by the conservation of momentum and mass, described by the equations:

$$\frac{\partial \mathbf{u}}{\partial t} + \mathbf{u} \cdot \nabla \mathbf{u} = -\nabla p + \frac{\beta}{Re} \nabla^2 \mathbf{u} + \frac{1-\beta}{Re} \nabla \cdot \boldsymbol{\tau}_p + f(t) \mathbf{e}_z, \quad \nabla \cdot \mathbf{u} = 0, \quad (2.1)$$

where \mathbf{u} and p represent non-dimensional velocity field and pressure field, respectively. The Reynolds number is defined as $Re = \rho U_c R / \eta$, where ρ and η are the density and zero-shear rate viscosity of the fluid. The pipe radius (R) and the Newtonian laminar centerline velocity (U_c) are the characteristic length and velocity scales, respectively. The viscosity ratio β represents the contribution of solvent viscosity (η_s) to the zero-shear solution viscosity and is defined as $\beta = \eta_s / \eta$. The contribution of polymer chains to the stress tensor in the momentum equation is denoted as $\boldsymbol{\tau}_p$, and we use the FENE-P constitutive equation having polymer molecular diffusion to model it (Bird *et al.* 1987):

$$\frac{\partial \boldsymbol{\alpha}}{\partial t} + \mathbf{u} \cdot \nabla \boldsymbol{\alpha} - \boldsymbol{\alpha} \cdot \nabla \mathbf{u} - (\boldsymbol{\alpha} \cdot \nabla \mathbf{u})^T = -\boldsymbol{\tau}_p + \frac{1}{ReSc} \nabla^2 \boldsymbol{\alpha}, \quad (2.2)$$

$$\boldsymbol{\tau}_p = \frac{1}{Wi} \left(\frac{\boldsymbol{\alpha}}{1 - \text{tr}(\boldsymbol{\alpha})/b} - \mathbf{I} \right), \quad (2.3)$$

where $\boldsymbol{\alpha}$, \mathbf{I} , and b are the conformation tensor, the identity tensor, and the maximum extensibility of the polymer chain, respectively. The Weissenberg number is defined as $Wi = \lambda U_c / R$, where λ is the polymer relaxation time. We keep the molecular diffusion in the evolution equation of the conformation tensor (Eq. 2.2) to ensure numerical stability. The strength of molecular diffusion is controlled by the Schmidt number $Sc = \eta / \rho D$, where D is the diffusion coefficient.

We perform numerical simulations for the axisymmetric pipe flow EIT. We consider non-slip boundary conditions on the wall of the pipe ($r = 1$) and axisymmetric boundary conditions at the center of the pipe ($r = 0$). The finite molecular diffusion of the polymer chains requires boundary conditions for the governing equation of the conformation tensor (Eq. 2.2). At the wall ($r = 1$), we solve Eq. 2.2 considering $1/Sc = 0$ and use the respective value of $\boldsymbol{\alpha}$ as the boundary condition. In the streamwise direction, we consider periodic boundary conditions. The volumetric flow through the pipe is kept constant at the Newtonian laminar value by tuning the body force ($f(t)$) at each time step.

We used *Dedalus* (Burns *et al.* 2020) to perform direct numerical simulations (DNS) using the spectral method. The length of computational domain is $L = 5 \times n$, where n is an integer. We used $256 \times n$ Fourier basis functions in the streamwise direction and 512 Chebyshev basis functions in the radial direction, respectively. We consider viscosity ratio $\beta = 0.97$ representing extreme dilute limit and $b = 6400$ corresponding to high molecular-weight polymer chains (500 kDa polyacrylamide). We consider molecular diffusion ($Sc = 250$) similar to the previous studies (Sid *et al.* 2018; Kumar & Graham 2024). The code validation can be found in the Appendix A. The simulations have been initiated with sufficiently large random perturbations in the state variables to trigger EIT. The simulation data corresponding to the initial 200 time units are dropped to make sure that the dynamics are fully developed.

2.2. VESPOD

To analyze the EIT dataset for pipe flow, we use a viscoelastic variant of SPOD (VESPOD), which allows the modal decomposition of the velocity and polymeric stress fields together. We note that the flow displays translation symmetry in the streamwise (z) direction, in which case the Fourier basis functions are optimal in terms of energy (Holmes *et al.* 2012). To embed this symmetry in our VESPOD framework, first, we Fourier-transformed state variables in the streamwise direction and then perform VESPOD decomposition wavenumber-by-wavenumber. The VESPOD represents the frequency-by-frequency VEPOD decomposition of a Fourier-transformed (in temporal direction) time-dependent dataset (Holmes *et al.* 2012; Wang *et al.* 2014), where VEPOD is a viscoelastic variant of POD (Kumar *et al.* 2025). Hence, VESPOD seeks to find the basis function $\boldsymbol{\psi}(\kappa, r, f)$ that maximizes the objective function

$$E\{|\langle \mathbf{q}(\kappa, r, f), \boldsymbol{\psi}(\kappa, r, f) \rangle|^2\} \quad (2.4)$$

given the constraint $\langle \boldsymbol{\psi}(\kappa, r, f), \boldsymbol{\psi}(\kappa, r, f) \rangle = 1$, where $E\{\cdot\}$ and $|\cdot|$ represent expectation and modulus operations, respectively. The quantity $\mathbf{q}(\kappa, r, f)$ represents a vector containing state variables having streamwise wavenumber per unit length of channel κ and temporal oscillation frequency f . In VESPOD, \mathbf{q} is defined as

$$\mathbf{q} = [\mathbf{u}', \mathbf{T}'], \quad (2.5)$$

where the stretch tensor $\mathbf{T} = \sqrt{\frac{1-\beta}{ReWi}} \boldsymbol{\theta}$ and $\boldsymbol{\theta} \cdot \boldsymbol{\theta} = \boldsymbol{\alpha}/(1 - \text{tr}(\boldsymbol{\alpha})/b)$ (Wang *et al.* 2014). The superscript ('') represents the perturbation from the mean (averaged over t and z). The inner

product $\langle \cdot, \cdot \rangle$ in the objective function (2.4) has been defined as:

$$\langle \mathbf{q}, \boldsymbol{\psi} \rangle = 2\pi \int_0^1 \mathbf{q}(r) \cdot \boldsymbol{\psi}(r) r dr. \quad (2.6)$$

The specific definition of variable \mathbf{q} leads to the following inner product of \mathbf{q} with itself:

$$\langle \mathbf{q}, \mathbf{q} \rangle = 2\pi \int_0^1 \left\{ \mathbf{u}' \cdot \mathbf{u}' + \frac{1-\beta}{ReWi} \boldsymbol{\theta}' : \boldsymbol{\theta}' \right\} r dr. \quad (2.7)$$

This inner product and choice of \mathbf{q} are chosen because in the limit $b \rightarrow \infty$, Eq. 2.7 becomes the total mechanical energy of the flow and is thus a natural and interpretable inner product for analysis of viscoelastic flows. In this limit, VESPOD yields an optimal decomposition in terms of total mechanical energy. For b finite, the identification with total mechanical energy is approximate but is nevertheless useful.

The maximization of the objective function (2.4) leads to the following self-adjoint eigenvalue problem:

$$2\pi \int_0^1 E\{\mathbf{q}(\kappa, r, f) \mathbf{q}^*(\kappa, \rho, f)\} \boldsymbol{\psi}(\kappa, \rho, f) \rho d\rho = \sigma \boldsymbol{\psi}(\kappa, r, f), \quad (2.8)$$

which gives an infinite set of eigenmodes $\{\sigma_j, \boldsymbol{\psi}_j(\kappa, r, f)\}$ which are arranged in decreasing value of (approximate) mechanical energy. The state variables can be reconstructed using VESPOD modes as

$$\tilde{\mathbf{q}}(\kappa, r, f) = \sum_{j=1}^{\infty} a_j(\kappa, f) \boldsymbol{\psi}_j(\kappa, r, f), \quad (2.9)$$

where $a_j(\kappa, f) = \langle \mathbf{q}(\kappa, r, f), \boldsymbol{\psi}_j(\kappa, r, f) \rangle$.

To obtain the VESPOD of a discrete time series, the data matrix containing the Fourier coefficients of the structures having wavenumber κ of the discrete time series of snapshots N_t is constructed as:

$$\mathbf{Q}_\kappa = [\mathbf{q}_{1,\kappa}, \mathbf{q}_{2,\kappa}, \dots, \mathbf{q}_{N_t,\kappa}], \quad (2.10)$$

where $\mathbf{q}_{i,\kappa} = \mathbf{q}(\kappa, r, t_i)$. The multiple realizations of the flow time series have been generated by dividing the data matrix into overlapping blocks as (Welch 1967)

$$\mathbf{Q}_\kappa^n = [\mathbf{q}_{1,\kappa}^n, \mathbf{q}_{2,\kappa}^n, \dots, \mathbf{q}_{m,\kappa}^n, \dots, \mathbf{q}_{N_f,\kappa}^n], \quad n = 1, 2, \dots, N_b, \quad (2.11)$$

where N_b and N_f are the number of blocks and the number of snapshots in each block. For N_o overlapping snapshots in each block, the entries of the data matrix \mathbf{Q}_κ^n and \mathbf{Q}_κ are related as $\mathbf{q}_{m,\kappa}^n = \mathbf{q}_{m+(n-1)(N_f-N_o),\kappa}$. Next, we compute the discrete Fourier transform (DFT) of each block in the temporal direction. To minimize the spectral leakage resulting from the non-periodicity of the data in each block during the estimation of the DFT, we compute the DFT of the windowed data:

$$\mathbf{Q}_\kappa^{n,w} = [w_1 \mathbf{q}_{1,\kappa}^n, w_2 \mathbf{q}_{2,\kappa}^n, \dots, w_m \mathbf{q}_{m,\kappa}^n, \dots, w_{N_f} \mathbf{q}_{N_f,\kappa}^n], \quad (2.12)$$

where w_m represents the nodal value of the symmetric Hamming window function and is given as:

$$w_m = 0.54 - 0.46 \cos \left(\frac{2\pi(m-1)}{N_f-1} \right). \quad (2.13)$$

The Fourier coefficients of the temporal DFT of $\mathbf{Q}_\kappa^{n,w}$ are given as

$$\tilde{\mathbf{Q}}_\kappa^n = [\tilde{\mathbf{q}}_{1,\kappa}^n, \tilde{\mathbf{q}}_{2,\kappa}^n, \dots, \tilde{\mathbf{q}}_{m,\kappa}^n, \dots, \tilde{\mathbf{q}}_{N_f,\kappa}^n], \quad (2.14)$$

where $\tilde{\mathbf{q}}_{m,\kappa}^n$ represents the Fourier coefficient of wavenumber κ at frequency f_m in the n^{th} block. Now, the Fourier coefficients at the frequency f_m are collected from each block and a new data matrix $\tilde{\mathbf{Q}}_{m,\kappa}$ is constructed as:

$$\tilde{\mathbf{Q}}_{m,\kappa} = [\tilde{\mathbf{q}}_{m,\kappa}^1, \tilde{\mathbf{q}}_{m,\kappa}^2, \dots, \tilde{\mathbf{q}}_{m,\kappa}^n, \dots, \tilde{\mathbf{q}}_{m,\kappa}^{N_b}]. \quad (2.15)$$

The VESPOD modes at the frequency f_m can be obtained by calculating the eigenmodes of the discretized cross-spectral density (CSD) matrix $\mathbf{S}_{m\kappa} = \tilde{\mathbf{Q}}_{m,\kappa} \tilde{\mathbf{Q}}_{m,\kappa}^*$ by solving the following eigenvalue problem:

$$\mathbf{S}_{m,\kappa} \mathbf{W} \psi_{m,\kappa} = \psi_{m,\kappa} \sigma_{m,\kappa}, \quad (2.16)$$

where $\psi_{m,\kappa} = \psi(\kappa, r, f_m)$ represents the VESPOD mode structures at wavenumber κ and frequency f_m , and diagonal matrix $\sigma_{m,\kappa}$ represents mechanical energy associated with respective mode structures. The matrix \mathbf{W} is a positive-definite weighting matrix, which properly accounts for the integration on a non-uniform discrete grid.

The eigenmode computation of (2.16) is expensive. To overcome this challenge, the following eigenvalue problem is solved:

$$\tilde{\mathbf{Q}}_{m,\kappa}^* \mathbf{W} \tilde{\mathbf{Q}}_{m,\kappa} \Theta_{m,\kappa} = \Theta_{m,\kappa} \sigma_{m,\kappa}. \quad (2.17)$$

This is faster to compute because the number of flow realizations (N_b) is much smaller than the number of grid points. This analogous problem gives the same nonzero eigenvalues as (2.16), and their eigenvectors are related as:

$$\psi_{m,\kappa} = \tilde{\mathbf{Q}}_{m,\kappa} \Theta_{m,\kappa} \sigma_{m,\kappa}^{-1/2}. \quad (2.18)$$

The VESPOD mode structures having wavenumber κ and frequency f_m can be projected in the physical space as:

$$\psi_m(z, r) = \psi_{m,\kappa} e^{i 2 \pi \kappa z / L}. \quad (2.19)$$

We modify the MATLAB tool originally developed by Schmidt (2022) to perform VESPOD analysis of EIT in pipe flow. We used data corresponding to 600 time units sampled at a time interval of $\Delta t_s = 0.025$ time units, leading to a total of 24000 snapshots. The multiple realizations of the flow have been constructed by dividing the data into blocks having $N_f = 2000$ snapshots in each block with 50% overlap. This leads to a total of 23 blocks, which is sufficient for a converged computation of VESPOD. The current choice of Δt_s and N_f leads to frequency resolution $\Delta f = 0.02$.

3. Results and discussion

We use VESPOD analysis to uncover the structures underlying the dynamics of EIT in axisymmetric pipe flow at several parameter regimes and domain lengths. First, we analyze dynamics at $Re = 3000$, $Wi = 35$, and $L = 5$ (Section 3.1). Then, we discuss dynamics of EIT in a longer domain ($L = 10$) (Section 3.2). Finally, we discuss the effect of Re and Wi on EIT (Section 3.3).

3.1. EIT at $Re = 3000$, $Wi = 35$, and $L = 5$

Figure 1 depicts the instantaneous snapshots of state variables and their temporal means for the dynamics of EIT at $Re = 3000$, $Wi = 35$, and $L = 5$. The dynamics of EIT has well-defined means (figure 1 (d, e)). Therefore, we report the perturbations of different state variables from their temporal means. The dynamics consists of weak velocity fluctuations, consistent with the nature of EIT (figure 1 (a, b)). The radial velocity field (u'_r) has distinct

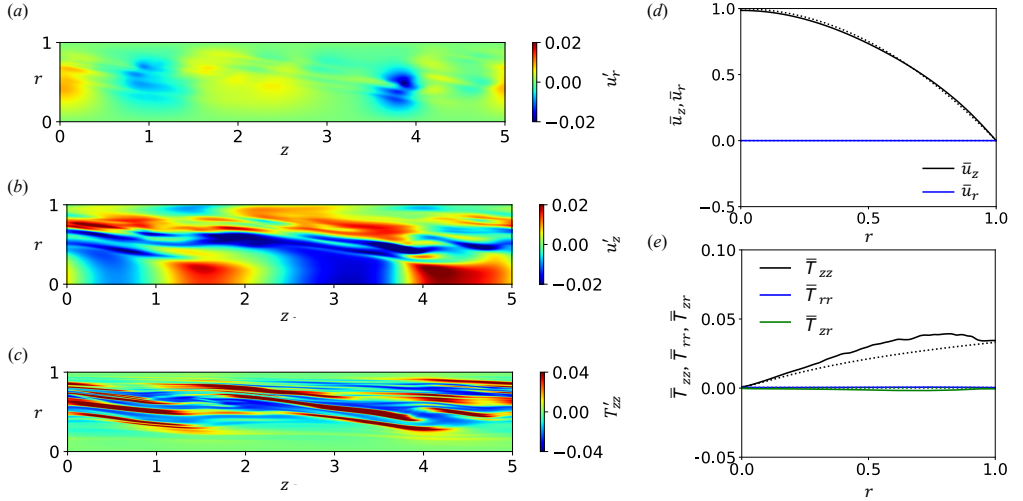


Figure 1: Instantaneous (a) radial velocity, (b) streamwise velocity, and (c) zz -component of stretch tensor of elastoinertial turbulence (EIT) in axisymmetric pipe flow at $Re = 3000$, $Wi = 35$, and $L = 5$. Means (averaged over z and t) of (d) velocity components and (e) stretch components. Dotted lines (d, e) represent the laminar profiles at the same parameter.

large-scale dynamic patterns dominating the region between the pipe centerline and the wall (figure 1a, movie 1). The streamwise velocity fluctuation (u'_z) has thin elongated streaks close to the wall; however, it contains large-scale structures in the vicinity of the pipe centerline (figure 1b, movie 2). The polymeric stress field contains the formation of thin sheets of high polymeric stress in the most part of the pipe with slight clustering near the pipe wall (Appendix B, movie 3). In the present paper, we use the scaled stretch field (\mathbf{T}) to represent polymeric stress field (figure 1c) and due to the appropriate scaling of the stretch field, which is based on its contribution to the mechanical energy, the velocity and stretch fields have similar magnitude (figure 1 (a–c)). This observation provides a quantitative evidence that for elastoinertial turbulence both inertia and elasticity are equally important. The zz -component of the polymeric stress (and stretch) tensor dominates the stress field. Therefore, we report only T'_{zz} in the present study. The stretch field (T'_{zz}) contains thin-inclined sheets of high stretch fluctuations situated well away from the pipe center $r = 0$ (figure 1c).

The VESPOD energy spectrum of the structures having wavenumber $\kappa = 1$ has been depicted in figure 2a. The leading eigenvalue (integrated over all frequencies) contributes approximately 78% to the total variance (approximate mechanical energy), and there are three distinct peaks in the leading eigenvalue, suggesting that the mode structures corresponding to these peaks have a large contribution to the overall dynamics. In figure 3, we visualize the mode structures corresponding to different peaks in the energy spectrum. The radial velocity component has large-scale structures located away from the pipe centerline, which move from the location close to the pipe wall for the peak at low frequency to the vicinity of the pipe centerline for the peak at high frequency (figure 3 (a–c)). The streamwise velocity component has large-scale structures centered at the pipe centerline, which shrink in the radial direction as the frequency of peak increases; however, it has elongated patches of velocity fluctuations close to the wall (figure 3 (d–f)). The stretch field contains a layer having thin inclined sheets of high stretch fluctuations, and the location of this layer moves to the centerline of the pipe as the frequency increases (figure 3 (g–i)). These three structures

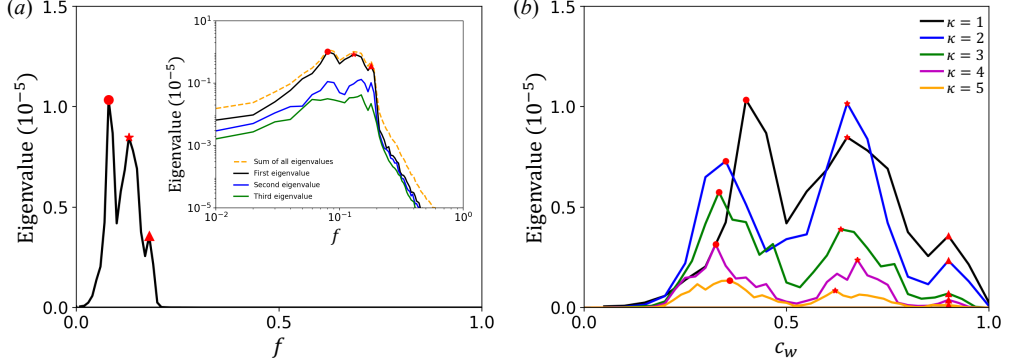


Figure 2: (a) Leading eigenvalue of the VESPOD energy spectrum of the structures having wavenumber $\kappa = 1$ underlying EIT at $Re = 3000$, $Wi = 35$, and $L = 5$ (Inset: spectrum in log-log scale). (b) Leading eigenvalues of the VESPOD energy spectra for structures having different wavenumbers. Red symbols represent the peaks in the leading eigenvalues (Circle ●, star ★, and triangle ▲ are first, second, and third peaks, respectively).

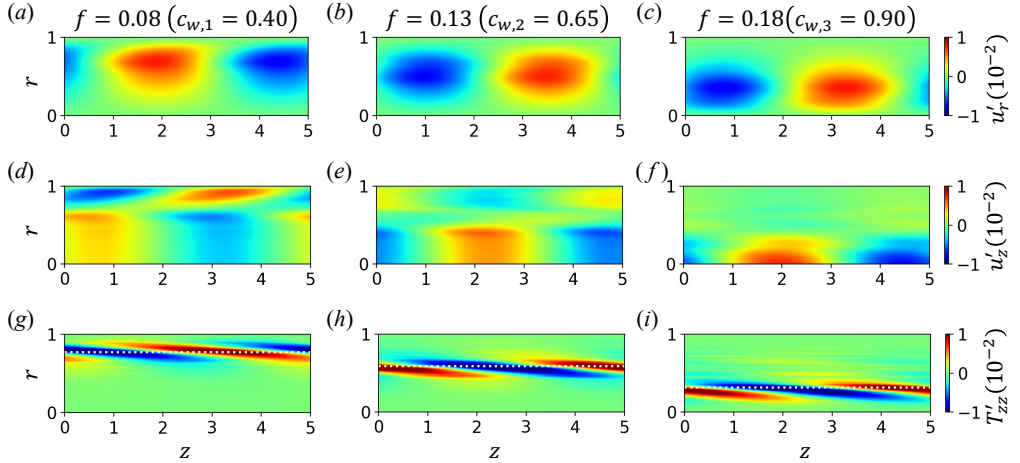


Figure 3: VESPOD mode structures of (a - c) radial velocity (u'_r), (d - f) streamwise velocity (u'_z), and (g - i) zz -component of stretch tensor (T'_{zz}) corresponding to the peaks in the leading eigenvalue of VESPOD energy spectrum of $\kappa = 1$. Locations of critical layers have been denoted with white dotted lines (g - i). Other parameters are $Re = 3000$, $Wi = 35$, and $L = 5$.

are distinct traveling waves; their wave speeds $c_w = fL/\kappa$ can be given as $c_{w,1}$, $c_{w,2}$, and $c_{w,3}$ in the ascending order of their wave speed, and corresponding peaks in the energy spectrum as peak index 1, 2, and 3, respectively.

The concept of critical layer has been proven useful in the understanding of transitional flows, as for traveling fluctuations it provides the most favorable place to exchange energy between the base flow and fluctuations (Drazin & Reid 1981). Therefore, we also explore the relationship between the critical layer of the traveling wave and the mode structures. As the mean velocity profile is close to the laminar parabolic profile (figure 1d), the location of the critical layer can be given as $r_c = \sqrt{1 - c_w}$. The sheets of high polymeric stretch fluctuations in the VESPOD modes are localized around the location of the critical layer (figure 3 (g-

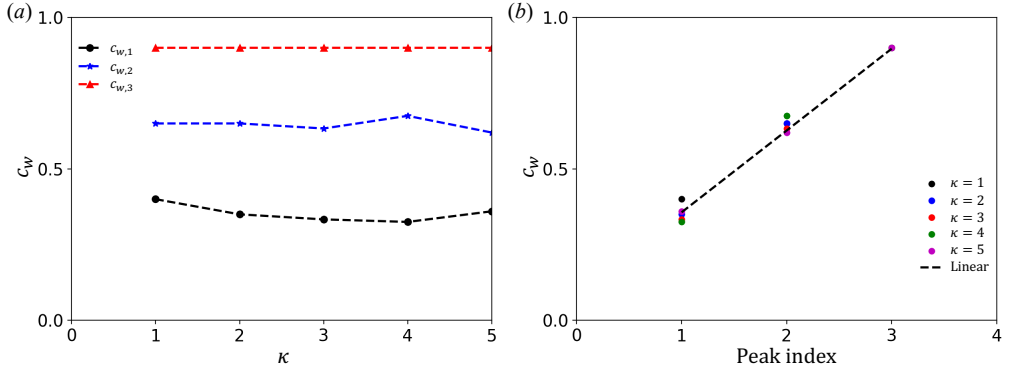


Figure 4: Wave speeds of the VESPOD mode structures corresponding to the peaks in the energy spectra: (a) Wave speed vs wave number and (b) Wave speed vs peak index. Parameter values are $Re = 3000$, $Wi = 35$, and $L = 5$.

i). This observation is consistent with the structures of traveling waves underlying EIT in channel flow (Shekar *et al.* 2019; Kumar & Graham 2024).

The VESPOD energy spectra of higher wavenumber structures have similar characteristics to those at $\kappa = 1$. The leading eigenvalues contain most of the energy across the spectra of different wavenumber structures and have three distinct peaks. In figure 2b, we visualize the leading eigenvalues of VESPOD corresponding to different κ as a function of wave speed. For a given peak index, the wave speeds of the mode structures are nearly independent of wavenumber, implying that the higher wavenumber structures ($\kappa \geq 2$) are simple harmonics of the fundamental wavenumber structure ($\kappa = 1$). This is also evident from figure 4. The traveling waves corresponding to each peak index belong to the respective unique family of traveling waves having unique wave speed (figure 4a), and the wave speed of the family of traveling waves increases almost linearly with the peak index (figure 4b).

In addition, we depict u'_r and T'_{zz} of mode structures corresponding to the three distinct peaks in the VESPOD energy spectra of higher wavenumber structures ($\kappa \geq 2$) in figures 5 and 6, respectively. The radial velocity component has large-scale structures, and these structures have a partition line oriented in the streamwise direction that divides the structures in two parts (figure 5). For each wavenumber, the location of the partition line moves to the centerline of the pipe as the wave speed increases. However, for a given wave speed (i.e., peak index), the location of the partition line is insensitive to the wavenumber. The stretch field is characterized by the formation of a layer, again localized at the critical layer position, having thin inclined sheets of high stretch fluctuations (figure 6). For a given wave speed, the locations of this layer for different wavenumber structures coincide with each other. However, they move to the pipe centerline as the wave speed increases for each wavenumber structure. Further, the location of partition line of the structure in radial velocity coincides with the critical layer, and hence the polymeric sheets.

The discussion so far demonstrates that the dynamics of EIT in pipe flow at $Re = 3000$, $Wi = 35$, and $L = 5$ is dominated by three distinct families of traveling waves, where higher wavenumber structures ($\kappa \geq 2$) originate from simple harmonic excitation of the fundamental wave ($\kappa = 1$). There also exist some relationships among different families of traveling waves. For example, the sheets of high polymeric stretch fluctuations of $c_{w,1}$ are located in the vicinity of the wall of the pipe and the polymeric stretch sheets of $c_{w,2}$ are confined in the region bounded by the pipe centerline and polymeric stretch sheets of $c_{w,1}$. Similarly, the sheets of $c_{w,3}$ are bounded by the pipe centerline and the sheets of

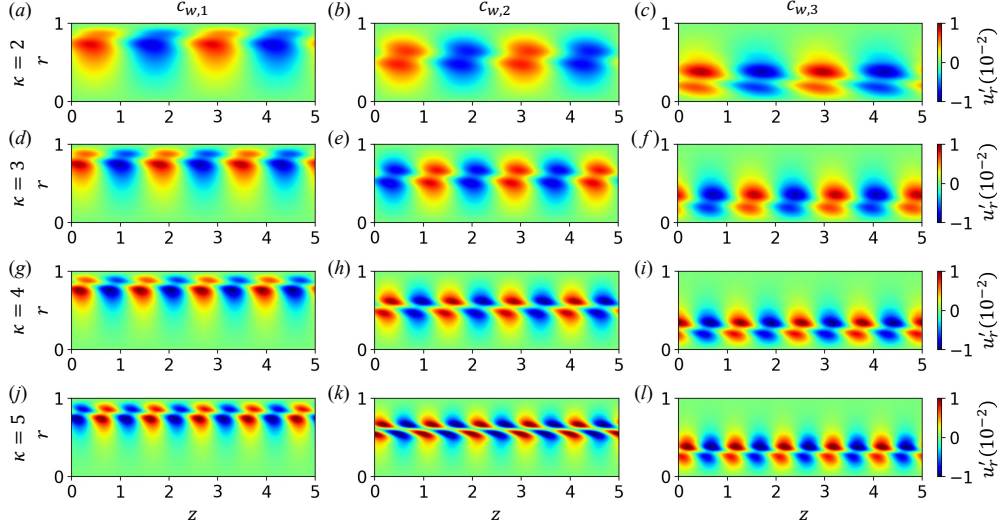


Figure 5: VESPOD mode structures of u'_r corresponding to different peaks in the leading eigenvalue of energy spectrum of wavenumber (a – c) $\kappa = 2$, (d – f) $\kappa = 3$, (g – i) $\kappa = 4$, and (j – l) $\kappa = 5$. Other parameters are $Re = 3000$, $Wi = 35$, and $L = 5$.

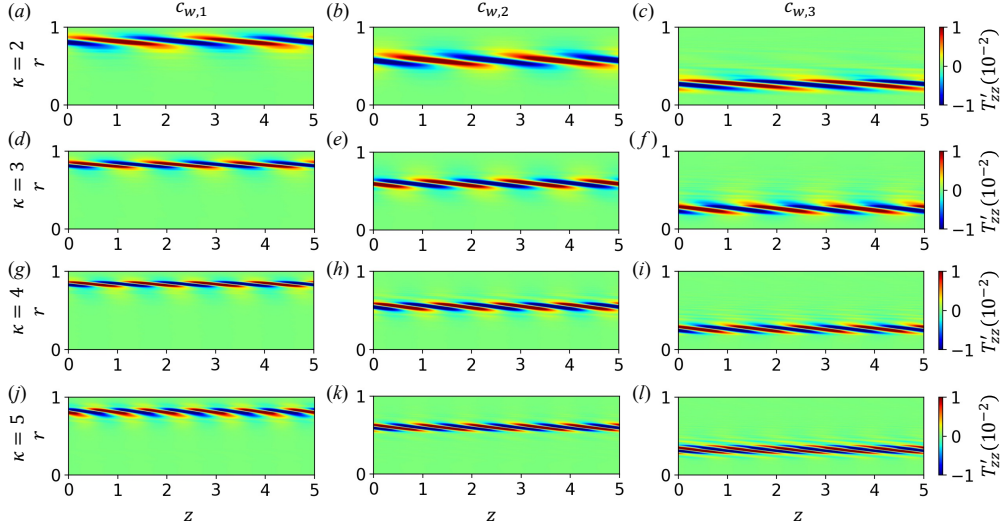


Figure 6: VESPOD mode structures of T'_{zz} corresponding to different peaks in the leading eigenvalue of energy spectrum of wavenumber (a – c) $\kappa = 2$, (d – f) $\kappa = 3$, (g – i) $\kappa = 4$, and (j – l) $\kappa = 5$. Other parameters are $Re = 3000$, $Wi = 35$, and $L = 5$. These structures correspond to the velocity structures shown in figure 5.

$c_{w,2}$. Thus, the polymeric sheets of different families of traveling waves exhibit a nested arrangement, where the polymeric sheets of faster waves are confined by the polymeric sheets of immediately slower waves. A similar nesting relationship among the dominant traveling waves underlying EIT in channel flow has been observed (Kumar & Graham 2024).

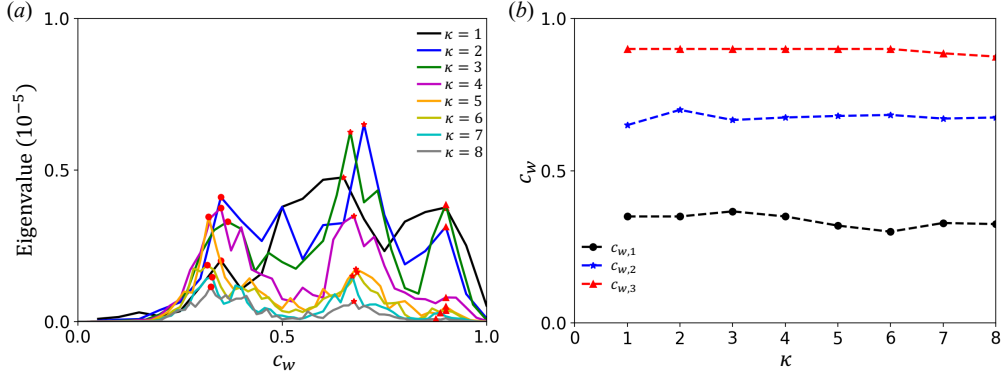


Figure 7: (a) Leading eigenvalues of the VESPOD energy spectra of different wavenumber structures at $Re = 3000$, $Wi = 35$, and $L = 10$. (b) Wave speeds of the traveling waves corresponding to the peaks in the leading eigenvalues of VESPOD energy spectra.

3.2. EIT at $Re = 3000$, $Wi = 35$, and $L = 10$

To explore the effect of pipe length on EIT dynamics, we performed a simulation in a domain twice the length of pipe discussed in Subsection 3.1, but at the same Re and Wi , and analyzed VESPOD energy spectra. The leading eigenvalue of the VESPOD spectrum of each wavenumber structure contains a dominant contribution to the total mechanical energy and has three distinct peaks similar to the shorter pipe. We visualize the leading eigenvalue of different wavenumber structures as a function of wave speed and find that the wave speeds corresponding to peaks in the leading eigenvalues are nearly independent of the wavenumber of structures (figure 7a). This shows that traveling waves with high wavenumber ($\kappa \geq 2$) are harmonics of the fundamental wave ($\kappa = 1$). This is also evident from figure 7b, where we see three distinct families of traveling waves originating from the simple harmonic excitation of respective fundamental waves. We have also visualized the structures of different traveling waves in figure 8. We would like to emphasize that the traveling waves having an even wavenumber ($\kappa = 2, 4, \dots$) in the pipe of $L = 10$ are the same traveling waves discovered in the pipe of $L = 5$. However, the traveling waves with an odd wavenumber ($\kappa = 1, 3, 5, \dots$) in the pipe of $L = 10$ are new and do not exist in the pipe of $L = 5$ because they do not satisfy the periodicity in the shorter domain. We also note that the energy associated with $\kappa = 2$ structures is higher than that of $\kappa = 1$ structures (at least for the first two families of traveling waves), suggesting that the structures having wavelength 5 units still dominate even in the pipe of $L = 10$ (figure 7a). This indicates that the pipe of $L = 5$ is long enough to capture the dominant structures.

3.3. Effect of Re and Wi

To explore the effects of Wi and Re on the dynamics of EIT, we analyze EIT at $(Re = 3000, Wi = 70, L = 5)$ (figure 9a) and $(Re = 6000, Wi = 35, L = 5)$ (figure 9b). The VESPOD energy spectrum at $(Re = 3000, Wi = 70)$ exhibits characteristics similar to those of the spectrum at $(Re = 3000, Wi = 35)$ (figures 9a and 2b). The three distinct harmonic families of traveling waves persist even at $Wi = 70$, evident from the three distinct peaks in the leading eigenvalues of the energy spectra of different wavenumber structures. For EIT at $Wi = 70$, the speeds of these three families of traveling waves are the same as the waves at $Wi = 35$, suggesting that Wi does not affect the speeds of different traveling waves at a fixed Re . At higher value of Wi , along with three harmonic peaks in the leading eigenvalues

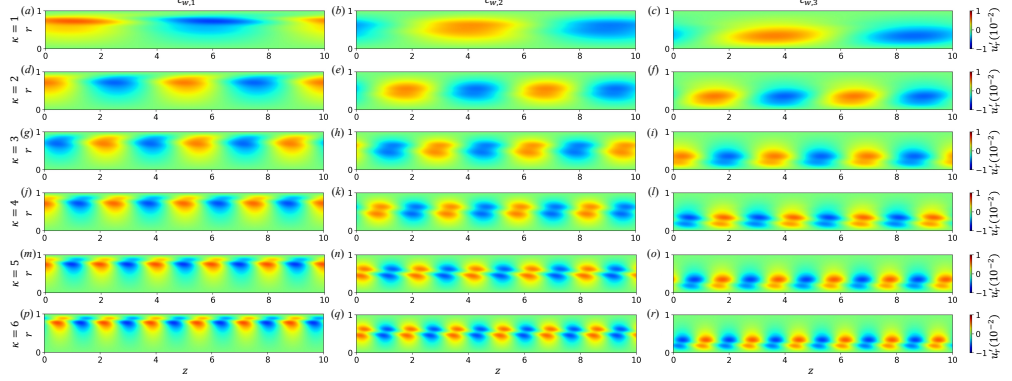


Figure 8: VESPOD mode structures of u'_r corresponding to different peaks in the leading eigenvalue of energy spectrum of different wave number structures in the pipe of length $L = 10$ ($Re = 3000$ and $Wi = 35$).

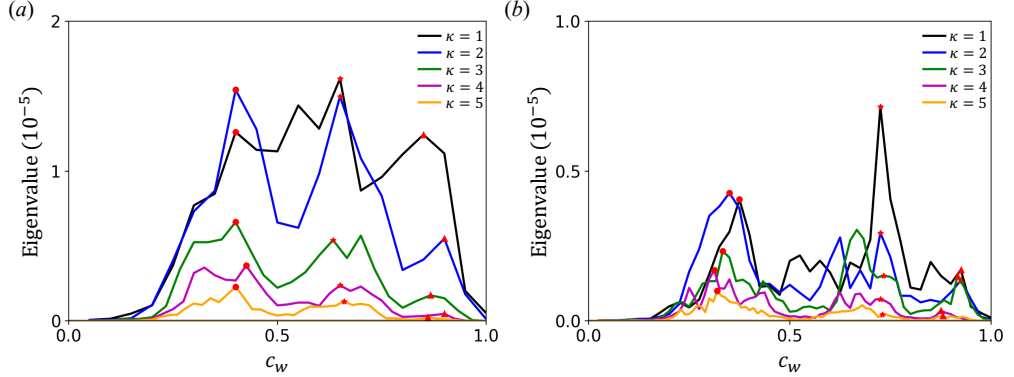


Figure 9: Leading eigenvalues of VESPOD energy spectra for different wavenumber structures at (a) $Re = 3000$, $Wi = 70$ and (b) $Re = 6000$, $Wi = 35$.

of VESPOD energy spectra, we also observe additional distinct peaks for some wavenumber structures (figure 9a). These are non-harmonic modes, having energy comparable to the harmonic modes. The mode structures corresponding to the peaks at $Wi = 70$ are similar to $Wi = 35$. Therefore, here we only include the structures corresponding to the first three peaks in the leading eigenvalue of $\kappa = 1$ at $Re = 3000$ and $Wi = 70$ (figure 10). The mode structures shown in figure 10 (a, d) and figure 10 (c, f) correspond to the fundamental wave of the first ($c_{w,1}$) and the second ($c_{w,2}$) families of harmonic traveling waves. However, the structures in figure 10 (b, e) correspond to the non-harmonic peak in the leading eigenvalue of the $\kappa = 1$ structure at $Re = 3000$ and $Wi = 70$ (figure 9a). We do not see any fundamental difference between the mode structures of the harmonic and non-harmonic peaks.

Further, we analyze dynamics at higher Re ($Re = 6000$), while keeping $Wi = 35$, same as in Subsection 3.1 (figure 9b). Again, there exist three dominant families of harmonic traveling waves. However, the speeds of the traveling waves at $Re = 6000$ are slightly different than those at $Re = 3000$. For example, the speed of the second family of traveling waves ($c_{w,2}$) at $Re = 6000$ is higher than that at $Re = 3000$. At larger Re , non-harmonic modes become increasingly important.

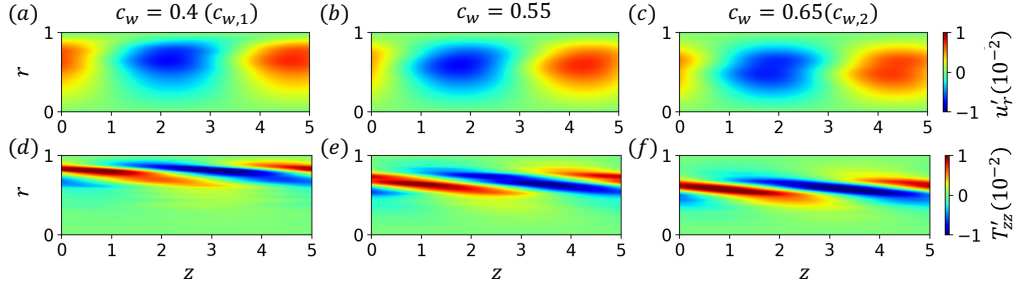


Figure 10: VESPOD mode structures of (a – c) u'_r and (d – f) T'_{zz} corresponding to the first three peaks in the leading eigenvalue of $\kappa = 1$ at $Re = 3000$ and $Wi = 70$. The middle column corresponds to the structures of the non-harmonic peak, however first and third columns represent harmonic peaks.

4. Conclusions

In the present study, we reveal the dominant well-defined structures underlying the dynamics of elastoinertial turbulence (EIT) in axisymmetric pipe flow using a viscoelastic variant of spectral proper orthogonal decomposition (VESPOD). The VESPOD enables us to perform modal decomposition of velocity and polymeric stress fields together and identify coherently evolving mode structures that contribute the most to the total mechanical energy of the dynamics of EIT. The leading eigenvalue of the VESPOD spectrum contains most of the mechanical energy and hence dominates its dynamics. The leading eigenvalue of the VESPOD energy spectrum of each wavenumber (κ) structure exhibits three distinct peaks. Further analysis of the mode structures corresponding to these peaks reveals three distinct families of well-defined traveling waves, which are characterized by their wave speed, dominate the dynamics of elastoinertial turbulence in axisymmetric pipe flow. The higher wavenumber structures ($\kappa \geq 2$) of each family of traveling wave are harmonics of their respective fundamental waves ($\kappa = 1$). The radial velocity component of these traveling waves contains large-scale structures spanning the radial direction, however the polymeric stress field contains thin-sheets of high stress fluctuations localized at the critical layers of the traveling waves. Further, the polymeric sheets of a given traveling wave confine the polymeric sheets of immediately faster wave, leading to a nested arrangement of the polymeric sheets. At larger values of the Reynolds numbers and Weissenberg numbers, along with three families of traveling waves, there also emerge non-harmonic traveling waves having energy content comparable to the harmonic waves.

The dynamics of EIT in channel and pipe flows share several similarities, but also exhibit important differences. Even though both dynamics have similar first glance features such as the large-scale structures in wall-normal velocity and the formation of thin inclined sheets of high stress in the polymeric stress field, the dominant coherent structures underlying them are distinct. EIT in channel flow is dominated by a family of non-harmonic traveling waves, whereas in pipe flow it is dominated by the three distinct families of harmonic traveling waves. The wall-normal velocity component of these traveling waves exhibits large-scale structures centered at the centerline in channel flow, whereas they are located away from the centerline in the pipe flow. The streamwise velocity component of these waves exhibits regular structures in the vicinity of the centerline in pipe flow, whereas in channel flow such distinct structures are located away from the centerline. However, the polymeric stress field in both channel and pipe flows contains sheets of high stress fluctuations at the critical layers of the traveling waves. Further, the polymeric sheets of faster traveling waves in both channel

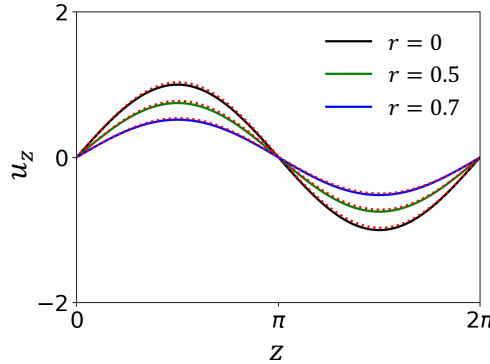


Figure 11: Exact (solid lines) and computed (dotted lines) profiles of u_z for a manufactured solution of viscoelastic flow through axisymmetric pipe at $Re = 3000$, $Wi = 35$, $\beta = 0.97$, and $b = 6400$.

and pipe flows are confined by the polymeric sheets of their immediately slower traveling waves, leading to a nested arrangement of polymeric sheets in both dynamics.

Acknowledgments

This research was supported under Office of Naval Research grant N00014-18-1-2865 (Vannevar Bush Faculty Fellowship) and National Science Foundation grant CBET-2437151.

Declaration of Interests

The authors report no conflict of interest.

Appendix A. Validation of numerical tool

We use the method of the manufactured solution for the validation of the numerical tool. We assume a solution having velocity and conformation tensor fields as:

$$u_z = (1 - r^2) \sin(z), \quad u_r = 0 \quad (\text{A } 1)$$

and

$$\alpha = (1 + \sin(z)) \mathbf{I}. \quad (\text{A } 2)$$

Next, we analytically obtain forcing functions to the governing equations (2.1 and 2.3) that satisfy the assumed solution (A 1 and A 2). Using these forcing terms, we perform a numerical simulation and compare the computed solution with the analytical solution and find an excellent agreement (figure 11).

Appendix B. Polymeric stress field for EIT in pipe flow

In the main text, we use the scaled stretch field to represent the stress resulting from the polymer. Figure 12 represents the instantaneous snapshot of the zz -component of the polymeric stress field for EIT in axisymmetric pipe flow.

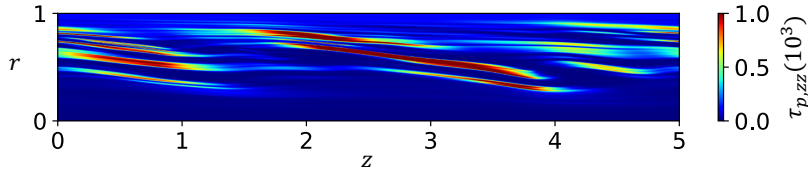


Figure 12: snapshot of the zz -component of the polymeric stress field for EIT in an axisymmetric pipe flow at parameter value $Re = 3000$, $Wi = 35$, and $L = 5$.

BENEITEZ, MIGUEL, PAGE, JACOB, DUBIEF, YVES & KERSWELL, RICH R. 2024a Multistability of elasto-inertial two-dimensional channel flow. *Journal of Fluid Mechanics* **981**, A30, arXiv: 2308.11554.

BENEITEZ, MIGUEL, PAGE, JACOB, DUBIEF, YVES & KERSWELL, RICH R. 2024b Transition route to elastic and elasto-inertial turbulence in polymer channel flows. *Physical Review Fluids* **9** (12), 123302, arXiv: 2408.11508.

BIRD, ROBERT BYRON, CURTISS, CHARLES F, ARMSTRONG, ROBERT C & HASSAGER, OLE 1987 *Dynamics of polymeric liquids, volume 2: Kinetic theory*. Wiley.

BURNS, K. J., VASIL, G. M., OISHI, J. S., LECOANET, D. & BROWN, B. P. 2020 Dedalus: A flexible framework for numerical simulations with spectral methods. *Physical Review Research* **2** (2), 023068.

CHAUDHARY, INDRESH, GARG, PIYUSH, SUBRAMANIAN, GANESH & SHANKAR, V. 2021 Linear instability of viscoelastic pipe flow. *Journal of Fluid Mechanics* **908**, A11, arXiv: 2003.09369.

CHOUEIJI, GEORGE H., LOPEZ, JOSE M., VARSHNEY, ATUL, SANKAR, SARATH & HOF, BJÖRN 2021 Experimental observation of the origin and structure of elastoinertial turbulence. *Proceedings of the National Academy of Sciences* **118** (45), 1–5, arXiv: 2103.00023.

DATTA, SUJIT S., ARDEKANI, AREZOO M., ARRATIA, PAULO E., BERIS, ANTONY N., BISCHOFBERGER, IRMGARD, MCKINLEY, GARETH H., EGGLERS, JENS G., LÓPEZ-AGUILAR, J. ESTEBAN, FIELDING, SUZANNE M., FRISHMAN, ANNA, GRAHAM, MICHAEL D., GUASTO, JEFFREY S., HAWARD, SIMON J., SHEN, AMY Q., HORMOZI, SARAH, MOROZOV, ALEXANDER, POOLE, ROBERT J., SHANKAR, V., SHAQFEH, ERIC S. G., STARK, HOLGER, STEINBERG, VICTOR, SUBRAMANIAN, GANESH & STONE, HOWARD A. 2022 Perspectives on viscoelastic flow instabilities and elastic turbulence. *Physical Review Fluids* **7** (8), 080701, arXiv: 2108.09841.

DRAZIN, PG & REID, WH 1981 *Hydrodynamic Stability* (Cambridge University).

DUBIEF, Y, PAGE, J, KERSWELL, R R, TERRAPON, V E & STEINBERG, V 2022 First coherent structure in elasto-inertial turbulence. *Physical Review Fluids* **7** (7), 073301.

DUBIEF, YVES, TERRAPON, VINCENT E & HOF, BJÖRN 2023 Elasto-Inertial Turbulence. *Annual Review of Fluid Mechanics* **55** (1), 675–705.

GARG, PIYUSH, CHAUDHARY, INDRESH, KHALID, MOHAMMAD, SHANKAR, V. & SUBRAMANIAN, GANESH 2018 Viscoelastic Pipe Flow is Linearly Unstable. *Physical Review Letters* **121** (2), 24502, arXiv: 1711.07991.

HOLMES, P., LUMLEY, J. L., BERKOOZ, G. & ROWLEY, C. W. 2012 *Turbulence, Coherent Structures, Dynamical Systems and Symmetry*, 2nd edn. Cambridge Monographs on Mechanics . Cambridge University Press.

KHALID, MOHAMMAD, CHAUDHARY, INDRESH, GARG, PIYUSH, SHANKAR, V. & SUBRAMANIAN, GANESH 2021 The centre-mode instability of viscoelastic plane Poiseuille flow. *Journal of Fluid Mechanics* **915**, A43, arXiv: 2008.00231.

KUMAR, MANISH, CONSTANTE-AMORES, C. RICARDO & GRAHAM, MICHAEL D. 2025 Elastoinertial turbulence: data-driven reduced-order model based on manifold dynamics. *Journal of Fluid Mechanics* **1007**, R1, arXiv: 2410.02948.

KUMAR, MANISH & GRAHAM, MICHAEL D. 2024 Nested travelling wave structures in elastoinertial turbulence. *Journal of Fluid Mechanics* **993**, A8, arXiv: 2403.06815.

KUMAR, MANISH, GUASTO, JEFFREY S. & ARDEKANI, AREZOO M 2023 Lagrangian stretching reveals stress topology in viscoelastic flows. *Proceedings of the National Academy of Sciences* **120** (5).

LEWY, THEO & KERSWELL, RICH R. 2025 Revisiting two-dimensional viscoelastic Kolmogorov flow: a centre-mode-driven transition. *Journal of Fluid Mechanics* **1007**, A55.

LOPEZ, JOSE M, CHOUEIJI, GEORGE H & HOF, BJÖRN 2019 Dynamics of viscoelastic pipe flow at low Reynolds numbers in the maximum drag reduction limit. *Journal of Fluid Mechanics* **874**, 699 – 719.

MOROZOV, ALEXANDER 2022 Coherent Structures in Plane Channel Flow of Dilute Polymer Solutions with Vanishing Inertia. *Physical Review Letters* **129** (1), 017801.

PAGE, JACOB, DUBIEF, YVES & KERSWELL, RICH R. 2020 Exact Traveling Wave Solutions in Viscoelastic Channel Flow. *Physical Review Letters* **125** (15), 154501, arXiv: 2006.08728.

SAMANTA, D., DUBIEF, Y., HOLZNER, M., SCHÄFER, C., MOROZOV, A. N., WAGNER, C. & HOF, B. 2013 Elasto-inertial turbulence. *PNAS* **110** (26), 10557–10562.

SCHMIDT, OLIVER T. 2022 Spectral proper orthogonal decomposition using multitaper estimates. *Theoretical and Computational Fluid Dynamics* **36** (5), 741–754, arXiv: 2112.10847.

SHEKAR, ASHWIN, McMULLEN, RYAN M., McKEON, BEVERLEY J. & GRAHAM, MICHAEL D. 2020 Self-sustained elastoinertial Tollmien–Schlichting waves. *Journal of Fluid Mechanics* **897**, A3, arXiv: 1910.11419.

SHEKAR, ASHWIN, McMULLEN, RYAN M., McKEON, BEVERLEY J. & GRAHAM, MICHAEL D. 2021 Tollmien–Schlichting route to elastoinertial turbulence in channel flow. *Physical Review Fluids* **6** (9), 093301, arXiv: 2104.10257.

SHEKAR, A., McMULLEN, R. M., WANG, S., McKEON, B. J. & GRAHAM, M. D. 2019 Critical-Layer Structures and Mechanisms in Elastoinertial Turbulence. *Physical Review Letters* **122** (12), 124503.

SID, S., TERRAPON, V. E. & DUBIEF, Y. 2018 Two-dimensional dynamics of elasto-inertial turbulence and its role in polymer drag reduction. *Physical Review Fluids* **3** (1), 011301, arXiv: 1710.01199.

TOMS, B. A. 1949 Some observations on the flow of linear polymersolutions through straight tubes at large reynolds numbers. In *Proc. 1st Intl Congr. Rheol.*, , vol. 2, pp. 135–141.

TOWNE, A., SCHMIDT, O. T. & COLONIUS, T. 2018 Spectral proper orthogonal decomposition and its relationship to dynamic mode decomposition and resolvent analysis. *Journal of Fluid Mechanics* **847**, 821–867.

VIRK, P S, MICKLEY, HAROLD S & SMITH, K A 1970 The ultimate asymptote and mean flow structure in Toms' phenomenon. *Journal of Applied Mechanics* **37** (2), 488–493.

WAN, DONGDONG, SUN, GUANGRUI & ZHANG, MENGQI 2021 Subcritical and supercritical bifurcations in axisymmetric viscoelastic pipe flows. *Journal of Fluid Mechanics* **929**, A16.

WANG, S., GRAHAM, M. D., HAHN, F. J. & XI, L. 2014 Time-series and extended Karhunen–Loève analysis of turbulent drag reduction in polymer solutions. *AIChE Journal* **60** (4), 1460–1475.

WELCH, P. 1967 The use of fast Fourier transform for the estimation of power spectra: A method based on time averaging over short, modified periodograms. *IEEE Transactions on Audio and Electroacoustics* **15** (2), 70–73.

Xi, Li 2019 Turbulent drag reduction by polymer additives: Fundamentals and recent advances. *Physics of Fluids* **31**, 121302.

ZHANG, MENGQI 2021 Energy growth in subcritical viscoelastic pipe flows. *Journal of Non-Newtonian Fluid Mechanics* **294** (February), 104581.

ZHANG, MENGQI, LASHGARI, IMAN, ZAKI, TAMER A. & BRANDT, LUCA 2013 Linear stability analysis of channel flow of viscoelastic Oldroyd-B and FENE-P fluids. *Journal of Fluid Mechanics* **737**, 249–279.